Published: IEEE Transactions on Dielectrics and Electrical Insulation Vol. 12, No. 1; February 2005

Cylindrical Geometry Electroquasistatic Dielectrometry Sensors

I. C. Shay (formerly Y. Sheiretov)
JENTEK Sensors, Inc.
110-1 Clematis Ave., Waltham, MA 02453, USA

and M. Zahn
Electrical Engineering Department
Massachusetts Institute of Technology
77 Massachusetts Ave., Room 10-174,
Cambridge, MA, 02139, USA

ABSTRACT

Semi-analytical models are used to simulate the response of periodic-field electroquasistatic dielectrometry sensors. Due to the periodic structure of the sensors it is possible to use Fourier transform methods in combination with collocation point numerical techniques to generate accurate sensor simulations much more efficiently than with the more general finite-element methods. The models previously developed for Cartesian geometry sensors have been extended to sensors with cylindrical geometry. This enables the design of families of circularly symmetric dielectrometers with the "model-based" methodology, which requires close agreement between actual sensor response and simulated response. These kinds of sensors are needed in applications where the components being tested have circular symmetry, or if it is important to be insensitive to sensor orientation, in cases where a property shows some anisotropy. It is possible to extend the Fourier Series Cartesian geometry models to this case with the use of Fourier-Bessel Series over a radius large compared to the sensor dimensions. The validity of the cylindrical geometry model is confirmed experimentally, where the combined response of two circularly symmetric dielectric sensors with different depths of sensitivity is used to simultaneously measure the permittivity of a dielectric plate and its lift-off from the electrode surface.

Index Terms — **Dielectrometer, electroquasistatic, cylindrical, Bessel series, parameter estimation.**

1 INTRODUCTION

CARTESIAN geometry interdigital electrode dielectrometry (IDED) sensors assume that: (1) the extent of the sensor is infinite in the y-direction with all physical quantities independent of y; and (2) the sensor extends to infinity in the x-direction and all physical quantities are spatially periodic in the x-direction with a wavelength λ [1, 2]. Whereas the second assumption is generally justified when guard electrodes are used near the two sides, the first assumption is justified only for impracticably long sensors.

A rotationally symmetric circular geometry sensor completely eliminates the y edge effect, because the counterpart of y in cylindrical coordinates is angle φ. The x edge effect, which corresponds to r in cylindrical coordinates, can also be minimized by making the radius R over which the Fourier-Bessel series is applied large compared to the relevant length scales. A further possible advantage of the rotationally symmetric sensors is their insensitivity to anisotropy of the material. Finally, certain structures, such as holes and fasteners, are by nature rotationally symmetric.

This paper presents mathematical models and numerical techniques used to calculate the response of sensors with rotational symmetry. It also shows experimental results that confirm the validity of the model.

Perhaps the most important difference between the semi-analytical modeling techniques for Cartesian and cylindrical geometry sensors is that the periodicity built into the Cartesian geometry sensors, which makes it possi-

Manuscript received on 27 October 2003, in final form 3 March 2004.

ble to use Fourier series methods efficiently, does not exist in cylindrical geometry. This is not to say that the idea of imposing a certain spatial quasi-periodicity in the r-direction as a way of controlling the effective depth of sensitivity no longer holds; on the contrary, this still is the main factor that influences the radii and spacing of the electrodes in the design of the sensors. In cylindrical coordinates Fourier-Bessel Series is used instead, but the radius R over which the Bessel Series is applied is chosen large compared to the characteristic lengths of the sensor. Choosing a large value for R, with the electrostatic potential forced to zero by a ground electrode for a significant fraction of the interval at its upper end, minimizes the effect of limiting the series expansion to a finite interval. As a consequence of choosing a large radius, terms in the series of much higher order must be included for the same numerical precision. This, coupled with the lack of convenient closed form product and summation formulas for Bessel functions, makes the computational burden much higher than the Cartesian coordinate methods.

2 MODELING

In the most common configuration, a measurement with an electroquasistatic dielectrometer is carried out with an impedance analyzer. The quantity being measured is the sensor transcapacitance, defined as

$$C_{\mathrm{T}} = \frac{I_{\mathrm{S}}}{i\omega V_{\mathrm{D}}} \tag{1}$$

where V_{D} is the complex magnitude of the voltage applied at one of the electrodes (the driven electrode) and I_{S} is the complex magnitude of the current that flows out of the other electrode (the sensing electrode), which is kept at ground potential. In the Cartesian geometry sensors the two electrodes form an interdigitated comb pattern [2] and are geometrically equivalent. In the case of the cylindrical geometry sensors, the driven electrode is a disk at the center, and the sensing electrode is formed as a sector of a concentric annulus, as shown in Figure 1. Using the center electrode as the drive has the advantage that several sensors with different effective depths of sensitivity, determined by the position of the sensing electrode, may be simulated simultaneously, as the electric field is identical for all cases.

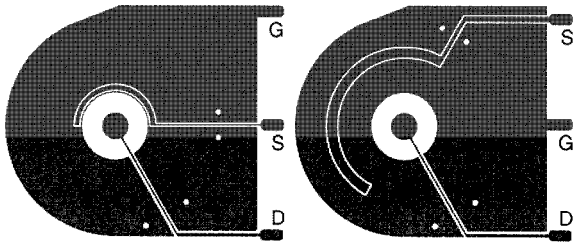

Figure 1. Layout of two circular dielectric sensors with different depths of sensitivity. Ignoring the effect of the narrow gap between the virtually grounded sensing electrode and the ground electrode, the electric field is identical for both sensors. The three electrodes are: driven ("D"), sensing ("S"), and ground ("G").

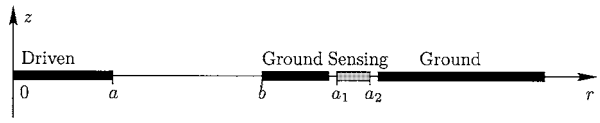

Figure 2. Definition of geometry parameters of a circular dielectrometer.

The goal of this method is to compute the sensor transcapacitance from the dielectric properties of the material under test and the geometric and dielectric properties of the sensor.

2.1 SENSOR GEOMETRY

A top view of the cylindrical geometry sensor is shown in Figure 1. A cross section of the sensor is shown in Figure 2, which also defines the geometrical parameters. In the analysis it is assumed that everywhere for $r \geq b$ the potential at $z = 0$ is forced to zero by the presence of a grounded metal plane. The sensing electrode is formed as a cut-out from this ground plane, with as small a gap as practically possible. It is kept at ground potential. The other side of the sensor substrate is also kept at ground via an electrode over the entire area of the sensor.

The value of the electrostatic potential at $z = 0$ is known for $0 \leq r \leq a$, where it is equal to the driving voltage, and for $r \geq b$, where it is zero. In the gap, it is determined via a collocation point method [1, 2].

2.2 COLLOCATION POINT METHOD

This method approximates the unknown potential in the gap as an interpolation between its values, ν_m, at a set of points, called the collocation points, in the interval $a < r_m < b$. The values ν_m are computed by solving a set of simultaneous equations, each of which is derived from a boundary condition applied over a spatial interval that contains the point r_m. For a more detailed discussion of this method, see [2]. An example of a potential function for a sensor in air, computed with this method, is shown in Figure 3.

In summary, the following steps are taken to compute the sensor transcapacitance from its geometry and the properties of the material under test:

- Solve Laplace's equation to determine the functional form of the electrostatic potential and the electric field intensity.
- Express the potential in the plane of the sensor by its values (to be determined) at a set of collocation points and a suitable interpolation function.
- Represent the potential as a Fourier series. Derive the series coefficients in terms of the potential values at the collocation points.

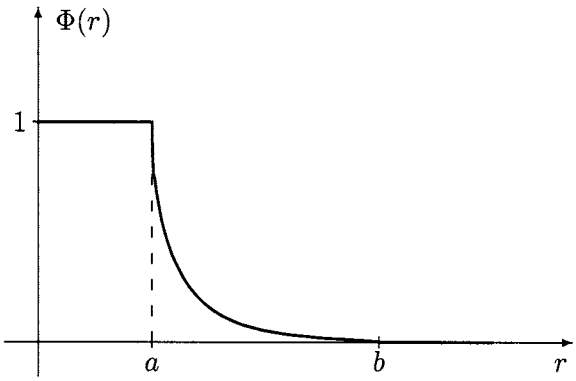

Figure 3. Normalized calculated potential at the electrode surface for the circular dielectrometer in air. In this case $a = 0.5$ mm, $b = 1.5$ mm, the substrate thickness is $h = 0.127$ mm, and its relative permittivity is $\epsilon_s = 2.1$.

- For each Fourier mode, compute the surface capacitance density, which relates the electric field intensity to the electrostatic potential, from the properties of the material under test.
- Apply boundary conditions over a set of spatial intervals containing the collocation points to obtain constraining equations. Solve the resulting linear system of equations.
- Use the thus obtained potential to compute the electric fields and integrate them over the sensing electrode area to compute the electrode terminal current.

2.3 LAPLACE EQUATION

Due to symmetry, the potential is independent of φ, i.e. $\Phi = \Phi(r,z)$. Laplace equation assumes the following form

$$\nabla^2\Phi = \frac{1}{r}\cdot\frac{\partial}{\partial r}\left(r\frac{\partial}{\partial r}\Phi\right) + \frac{\partial^2}{\partial z^2}\Phi = 0 \qquad (2)$$

The relevant solution of this differential equation is

$$\Phi(r, z) = J_0(\beta r)\left(c_1 e^{-\beta z} + c_2 e^{+\beta z}\right) \qquad (3)$$

The other solution that uses the Bessel function Y_0 is not applicable in this case because Y_0 is infinite at $r = 0$, while the potential must remain finite. For the solution in equation (3) the electric field is given by

$$\mathbf{E} = -\nabla\Phi = \beta J_1(\beta r)\left(c_1 e^{-\beta z} + c_2 e^{+\beta z}\right)\hat{\mathbf{r}} + \beta J_0(\beta r)\left(c_1 e^{-\beta z} - c_2 e^{+\beta z}\right)\hat{\mathbf{z}} \qquad (4)$$

Equation (3) implies that the appropriate Fourier series to use to express the potential is the Bessel series based on J_0 [3]

$$f(r) = \sum_{n=1}^{\infty} A_n J_0\left(\frac{\alpha_n}{R}r\right) \qquad 0 < r < R \qquad (5)$$

where α_n here are the positive real zeros of J_0. The zeros are indexed from one, i.e. $\alpha_1 = 2.405$. Correspondingly, the coefficients A_n are given by

$$A_n = \frac{1}{Q_n}\int_0^R rf(r)J_0\left(\frac{\alpha_n}{R}r\right)dr \qquad (6)$$

where

$$Q_n = \int_0^R rJ_0^2\left(\frac{\alpha_n}{R}r\right)dr = \frac{R^2}{2}J_1^2(\alpha_n) \qquad (7)$$

The radius R is the outer limit of the interval over which the Bessel series expansion is applied. The series expansion is valid only over the interval $0 \le r \le R$ and will produce incorrect results if used to compute the potential for $r > R$ and consequently the electric field in the vicinity of and beyond R. For this reason, R must be chosen to be several times greater than the characteristic size of the sensor, i.e $R \gg a_2$.

2.4 COLLOCATION POINTS

In the sensor gap the electrostatic potential is approximated by an interpolation of its value between a set of $K+2$ collocation points, r_m. The first and last points are at the electrode edges, where the potential is known. In the gap the points are concentrated near the edges, where the potential is changing most rapidly, as illustrated in Figure 3. For the same reason the collocation points are more heavily concentrated near the driven electrode, according to the following formula

$$r_m = a\frac{b-a}{2}\left\{1 - \cos\left(\frac{m\pi}{K+1}\right) + 0.15\left[\cos\left(\frac{2m\pi}{K+1}\right) - 1\right]\right\} \qquad m = 0,1,2,\ \ldots,\ K+1 \qquad (8)$$

A fraction of the second harmonic is added to the traditionally used cosinusoidal distribution [2], in order to skew the points toward the driven electrode. Figure 4 shows the resulting positions of the collocation points. The integration intervals, over which the boundary conditions are applied, are delimited by r_m^*, which are interleaved with

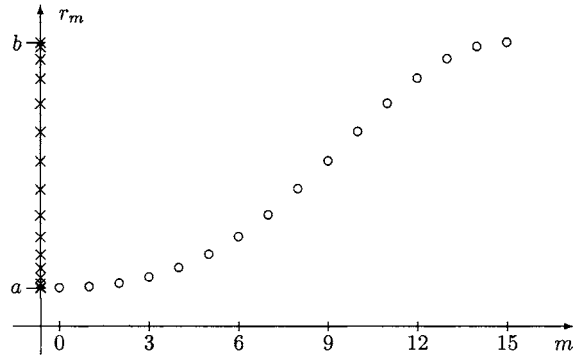

Figure 4. Positions of 16 collocation points. The points are concentrated near the electrode edges, at $r = a$ and $r = b$ where the potential is changing most rapidly. The concentration is skewed toward the driven electrode. The crosses (×) on the ordinate illustrate the collocation point positions on the *r*-axis.

r_m and are positioned half way between the collocation points, except at the two ends

$$r_m^* = \begin{cases} r_0 & m = 0 \\ r_{K+1} & m = K \\ (r_{m+1} + r_m)/2 & m = 1,2, \ldots, K-1 \end{cases} \quad (9)$$

A suitable interpolation function must be chosen to express Φ as a function of its values at the collocation points. To find this function consider the following: integrals of the form $\int r^p J_0(r) dr$ have closed form solutions when p is an odd integer. For example

$$\int r J_0(r)\, dr = r J_1(r)$$
$$\int r^3 J_0(r)\, dr = r^3 J_1(r) - 2r^2 J_2(r) \quad (10)$$

In order to make it possible to evaluate the integral in equation (6) in closed form, an appropriate and sufficiently simple interpolation function therefore is of the form $c_1 + c_2 r^2$, which results in the following interpolation function $\nu(r)$ for the potential in the interval between r_m and r_{m+1}

$$\nu = \frac{\nu_m\left(r_{m+1}^2 - r^2\right) + \nu_{m+1}\left(r^2 - r_m^2\right)}{r_{m+1}^2 - r_m^2} \quad (11)$$

Using equations (11) and (6), it is possible to express the Bessel series coefficients Φ_n in the expansion of the potential $\Phi(r)$ over the period $0 \le r \le R$ in terms of the potential values ν_m as follows

$$\Phi_n = \frac{1}{Q_n}\left[\int_0^a r J_0(\beta_n r)\, dr + \sum_{m=0}^{K} \int_{r_m}^{r_{m+1}} r J_0(\beta_n r) \times \frac{\nu_m\left(r_{m+1}^2 - r^2\right) + \nu_{m+1}\left(r^2 - r_m^2\right)}{r_{m+1}^2 - r_m^2} dr\right] \quad (12)$$

where the coefficients Φ_n are defined in equation (7) and $\beta_n = \alpha_n/R$. The first term in equation (12) results from integration over the driven electrode, where the potential is constrained to be equal to the driving voltage V_D. Since the potential everywhere scales proportionally with V_D, it may be set to unity for convenience. The potential is zero for $r \ge b$ and therefore this interval does not contribute to the integral. Carrying out the integration yields

$$\Phi_n Q_n \beta_n^2 = \beta_n a J_1(\beta_n a) + 2\sum_{m=0}^{K} \frac{\nu_m - \nu_{m+1}}{r_{m+1}^2 - r_m^2}\left[r_{m+1}^2 J_2(\beta_n r_{m+1}) - r_m^2 J_2(\beta_n r_m)\right] + \beta_n \sum_{m=0}^{K} \left[\nu_{m+1} r_{m+1} J_1(\beta_n r_{m+1}) - \nu_m r_m J_1(\beta_n r_m)\right] \quad (13)$$

The terms in the second summation of equation (13) cancel each other on a term by term basis, except for the two end terms multiplying ν_0 and ν_{K+1}. The latter is at $r_{K+1} = b$, where the potential is zero and can be ignored. The first one contributes a term equal to $-\beta_n a J_1(\beta_n a)$, which exactly cancels the leading term in equation (13). This results in a much simpler expression

$$\Phi_n = \frac{4}{\alpha_n^2 J_1^2(\alpha_n)} \sum_{m=0}^{K} \frac{\nu_m - \nu_{m+1}}{r_{m+1}^2 - r_m^2} \times \left[r_{m+1}^2 J_2(\beta_n r_{m+1}) - r_m^2 J_2(\beta_n r_m)\right] \quad (14)$$

which can be rewritten as

$$\Phi_n = \frac{4}{\alpha_n^2 J_1^2(\alpha_n)}\left\{\frac{r_1^2 J_2(\beta_n r_1) - r_0^2 J_2(\beta_n r_0)}{r_1^2 - r_0^2} + \sum_{m=1}^{K} \nu_m \left[\frac{r_{m+1}^2 J_2(\beta_n r_{m+1}) - r_m^2 J_2(\beta_n r_m)}{r_{m+1}^2 - r_m^2} - \frac{r_m^2 J_2(\beta_n r_m) - r_{m-1}^2 J_2(\beta_n r_{m-1})}{r_m^2 - r_{m-1}^2}\right]\right\} \quad (15)$$

in order to consolidate the coefficients multiplying ν_m. Note that in equation (15) the index of the summation starts at $m = 1$. The first term has been written out separately, because $\nu_0 = 1$ is known.

2.5 SURFACE CAPACITANCE DENSITY

There are two parameters of a medium that determine the quasistatic distribution of electric fields: the dielectric permittivity ϵ and the conductivity σ. The former determines the displacement current density from the electric field, while the latter relates the conduction current density to the electric field. The permittivity governs energy storage (reactive power) phenomena, while the conductivity determines the power dissipation (active power). It is possible to combine these two effects by adding the effect of the ohmic conductivity to the imaginary (loss) component of the complex permittivity.

Consider an electrode in contact with a medium as shown in Figure 5. In the one-dimensional geometry in the figure, the current density and the electric field are perpendicular to the electrode. Let the normal component of the electric field at the electrode surface be E. The terminal current I can be obtained by integrating the total current per unit electrode area J that flows into the electrode. The total current density is given by

$$J = J_C + J_D = \sigma E + \frac{d}{dt}(\epsilon E) \quad (16)$$

where J_C is the conduction current density and J_D is the displacement current density.

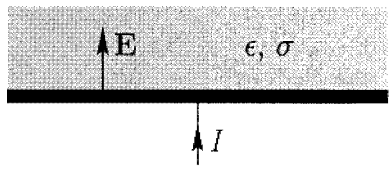

Figure 5. Terminal current of an electrode in contact with a conducting dielectric medium.

Under sinusoidal steady state operation at angular frequency ω equation (16) becomes

$$J = J_C + J_D = \sigma E + i\omega\epsilon E = i\omega E\left(\epsilon + \frac{\sigma}{i\omega}\right) \quad (17)$$

where $i = \sqrt{-1}$. Consequently it is possible to include conduction loss in analyses that otherwise consider only insulating dielectrics simply by replacing ϵ in a medium with the corresponding *complex permittivity* ϵ^*, *defined as*

$$\epsilon^* = \epsilon' - i\epsilon'' = \epsilon - i\frac{\sigma}{\omega} \quad (18)$$

This makes it possible to rewrite equation (17) as

$$J = i\omega\epsilon^* E \quad (19)$$

For a particular spatial Fourier-Bessel mode n many quantities have the same J_0 dependence on r. It is therefore convenient to adopt the following notation, assigning the tilde ($\sim$) accent to imply the r-dependence of any quantity F

$$F_n(r,z) = \tilde{F}_n(z) J_0(\beta_n r) \quad (20)$$

Using $\mathbf{E} = -\nabla\Phi$, the normal electric field intensity can be expressed in terms of the potential as $E_{z,n}(r,z) = -(\partial/\partial z)\Phi_n(r,z)$, which, using this notation, can be written in abbreviated form as

$$\tilde{E}_{z,n}(z) = -\frac{d}{dz}\tilde{\Phi}_n(z) \quad (21)$$

Consider a material structure with several homogeneous layers, as shown in Figure 6. The top layer borders on a ground plane. This is a good model even if no such electrode is present in an experimental setup, since there are many objects in the vicinity which are at ground potential, which act as a ground at a certain effective distance [1]. In fact, it is better to explicitly place a grounded metal plate behind the material under test, so that it is at a controlled distance to be used in the model. Nonetheless, it is still possible to model a structure with no ground plane by letting the thickness of the top layer approach infinity.

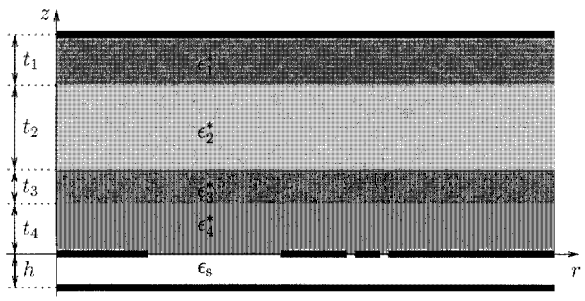

Figure 6. Material structure with several layers of homogeneous materials.

In the electroquasistatic regime it is possible to define the *complex surface capacitance density* as

$$C_n^*(z) = \frac{1}{\beta_n} \cdot \frac{\epsilon^*(z)\tilde{E}_{z,n}(z)}{\tilde{\Phi}_n(z)} \quad (22)$$

In terms of its effect on the sensor transcapacitance, all information about the material under test is contained in the value of $C_n^*(z)$ at $z = 0$ for all spatial Fourier-Bessel modes. Note that $\epsilon^*(z)\tilde{E}_{z,n}(z)$, $\tilde{\Phi}_n(z)$, and therefore $C_n^*(z)$, are continuous in the z-direction at material interfaces with no electrodes.

The goal is to compute C_n^* at the bottom of the stack shown in Figure 6. First consider a homogeneous material layer (i.e. ϵ^* is constant) that extends to infinity in the positive z-direction, with bottom interface at $z = z_0$. Out of the solutions in equation (3), only the $e^{-\beta z}$ term remains finite at $z = \infty$, leading to

$$\tilde{\Phi}_n(z) = \tilde{\Phi}_n(z_0) e^{-\beta_n(z - z_0)} \quad (23)$$

and

$$\tilde{E}_{z,n}(z) = \beta_n \tilde{\Phi}_n(z_0) e^{-\beta_n(z - z_0)} \quad (24)$$

Consequently, at the bottom interface of such an infinitely thick layer,

$$C_n^*(z_0) = \epsilon^* \quad (25)$$

The next step is to relate C_n^* at the bottom interface ($z = z_0$) of a layer of thickness t to its value at the upper interface ($z = z_0 + t$). In regions of finite thickness it is more convenient to work with the hyperbolic function equivalent of equation (3)

$$\Phi = J_0(\beta r)\left[c_1 \sinh(\beta z) - c_2 \cosh(\beta z)\right] \quad (26)$$

making it possible to express the potential in the layer in terms of its values at the two interfaces as

$$\tilde{\Phi}_n(z) = \frac{1}{\sinh(\beta_n t)}\left[\tilde{\Phi}_n(z_0 + t)\sinh\beta_n(z - z_0) - \tilde{\Phi}_n(z_0)\sinh\beta_n(z - z_0 - t)\right] \quad (27)$$

Applying equations (21) and (22) to equation (27) yields the following equations for $C_n^*(z)$ at the two interfaces

$$C_n^*(z_0) = -\epsilon^*\left[\frac{\tilde{\Phi}_n(z_0 + t)}{\tilde{\Phi}_n(z_0)} \cdot \frac{1}{\sinh(\beta_n t)} - \coth(\beta_n t)\right]$$

$$C_n^*(z_0 + t) = -\epsilon^*\left[\coth(\beta_n t) - \frac{\tilde{\Phi}_n(z_0)}{\tilde{\Phi}_n(z_0 + t)} \cdot \frac{1}{\sinh(\beta_n t)}\right] \quad (28)$$

from which the ratio $\tilde{\Phi}_n(z_0 + t)/\tilde{\Phi}_n(z_0)$ can be eliminated to arrive at the following transfer relation

$$C_n^*(z_0) = \epsilon^* \frac{C_n^*(z_0 + t)\coth(\beta_n t) + \epsilon^*}{C_n^*(z_0 + t) + \epsilon^*\coth(\beta_n t)} \quad (29)$$

Thus it is possible to calculate $C_n^*(z=0)$ in the plane of the electrodes by starting with the infinite half-space layer that is furthest from the electrodes, using equation (25), and then sequentially applying equation (29) across each layer until the electrode surface is reached.

The surface capacitance density at a layer surface a distance t below the top ground plane, such as the one shown in Figure 6, can be computed from equation (29) by taking the limit where $C_n(z_0+t)\to\infty$, since $\Phi_n(z_0+t)=0$ at the top interface in contact with the ground plane

$$C_n^*(z_0)=\epsilon^*\coth(\beta_n t)\quad n>0 \tag{30}$$

which approaches ϵ^* at sufficiently large values of the thickness t, in agreement with equation (25).

The quantity σ_S^* is defined as the jump in the normal component of $\epsilon^*\mathbf{E}$ across an interface, $\sigma_S^*(r)=\|\epsilon^* E_z(r)\|$. It would be equal to the surface charge density in the absence of ohmic conduction in the medium. It is zero at every interface except in the plane of the electrodes. Using equation (22), for every Fourier-Bessel mode σ_S^* is related to the difference in surface capacitance density above and below the electrodes, $C_n^*\equiv\|C_n^*(z)\|$, as

$$\sigma_{Sn}^*=C_n^*\beta_n\Phi_n \tag{31}$$

where σ_{Sn}^* are the coefficients of the Bessel series expansion of $\sigma_S^*(r)$. The jump in the normal component of the total current density can be expressed in terms of $\sigma_S^*(r)$ via equation (19):

$$\|J_z(r)\|=i\omega\sigma_S^*(r) \tag{32}$$

2.6 BOUNDARY CONDITIONS

The relevant boundary condition in the gap between electrodes is

$$\sigma_S^*(r)=0 \tag{33}$$

which results from equation (32), since there is no electrode to act as a current source or sink, and no surface conduction is considered. If surface conductivity and permittivity are present, they may be incorporated in the model by introducing an additional material layer and taking the limit as its thickness approaches zero. The integral of the condition in equation (33), over every interval $r_m^*<r<r_{m+1}^*$, is

$$\begin{aligned}\int_{r_m^*}^{r_{m+1}^*}\sigma_S^*(r)2\pi r\,dr&=\sum_{n=1}^{\infty}\int_{r_m^*}^{r_{m+1}^*}C_n^*\Phi_n\beta_n J_0(\beta_n r)2\pi r\,dr\\&=2\pi\sum_{n=1}^{\infty}C_n^*\Phi_n\left[r_{m+1}^*J_1(\beta_n r_{m+1}^*)-r_m^*J_1(\beta_n r_m^*)\right]\\&=\sum_{n=1}^{\infty}C_n^*\sum_{j=0}^{K}M_{m,j}^n\nu_j=0\end{aligned} \tag{34}$$

The last line in equation (34) comes from substituting equation (15) into the equation and grouping together the terms multiplying ν_m into the coefficient matrix M^n.

One equation results from the application of the boundary condition over each of the integration intervals. In matrix form this set of equations can be written as $M\mathbf{v}=\mathbf{x}$, where $\mathbf{v}$ is a vector of the unknown potential values ν_m. The matrix M can be derived from equation (34)

$$M=\sum_{n=1}^{\infty}C_n^*M^n \tag{35}$$

The advantage of formulating M as a summation of the sub-matrices M^n is that the sub-matrices depend only on the sensor parameters, and need to be computed once when calculating the sensor response for a variety of material properties and geometries, where each configuration has a different set of C_n^*. After substituting equation (15) into equation (34), the elements of M^n are determined to be

$$\begin{aligned}M_{m,j}^n=\frac{8\pi}{\alpha_n^2J_1^2(\alpha_n)}&\left[r_{m+1}^*J_1(\beta_n r_{m+1}^*)-r_m^*J_1(\beta_n r_m^*)\right]\\&\times\left[\frac{r_{j+1}^2J_2(\beta_n r_{j+1})-r_j^2J_2(\beta_n r_j)}{r_{j+1}^2-r_j^2}\right.\\&\left.-\frac{r_j^2J_2(\beta_n r_j)-r_{j-1}^2J_2(\beta_n r_{j-1})}{r_j^2-r_{j-1}^2}\right]\end{aligned} \tag{36}$$

The right hand side vector $\mathbf{x}$ of the matrix equation can similarly be expressed as a summation over Fourier modes

$$\mathbf{x}=\sum_{n=1}^{\infty}C_n^*\mathbf{x}^n \tag{37}$$

Extracting the appropriate constant terms from equation (15) gives for the mth element of the vector $\mathbf{x}^n$

$$\begin{aligned}x_m^n=-\frac{8\pi}{\alpha_n^2J_1^2(\alpha_n)}&\cdot\frac{r_1^2J_2(\beta_n r_1)-r_0^2J_2(\beta_n r_0)}{r_1^2-r_0^2}\\&\times\left[r_{m+1}^*J_1(\beta_n r_{m+1}^*)-r_m^*J_1(\beta_n r_m^*)\right]\end{aligned} \tag{38}$$

Solving the matrix equation results in full knowledge of the electrostatic potential $\Phi(r)$ at the electrode surface. Figure 3 shows this function for a dielectric sensor in air.

2.7 CALCULATING TRANSCAPACITANCE

The transcapacitance is obtained by calculating the terminal current I_S in equation (1). The terminal current is equal to the integral over the sensing electrode area of the jump in the normal component of the total current density, $\|J_z(r)\|$. Using equation (32), the transcapaci-

tance is computed by integrating σ_s^* over the sensing electrode area

$$C_T = -\sum_{n=1}^{\infty} \int_{a_1}^{a_2} C_n^* \Phi_n \beta_n J_0(\beta_n r)\, \theta r\, dr$$

$$= -\theta \sum_{n=1}^{\infty} C_n^* \Phi_n \left[a_2 J_1(\beta_n a_2) - a_1 J_1(\beta_n a_1) \right] \quad (39)$$

where the electrode extends from a_1 to a_2 radially and has an arc angle of θ, which for practical sensors must be less than 2π. In Figure 1 both sensors have $\theta = \pi$, i.e. 180°.

In order to express the transcapacitance C_T in terms of the vector of potential values ν_m calculated in the last step, equation (15) is substituted into equation (39), yielding

$$C_T = -4\theta \sum_{n=1}^{\infty} \frac{C_n^*}{\alpha_n^2 J_1^2(\alpha_n)} \left[a_2 J_1(\beta_n a_2) - a_1 J_1(\beta_n a_1) \right] \times \left\{ \frac{r_1^2 J_2(\beta_n r_1) - r_0^2 J_2(\beta_n r_0)}{r_1^2 - r_0^2} + \sum_{m=1}^{K} \nu_m \left[\frac{r_{m+1}^2 J_2(\beta_n r_{m+1}) - r_m^2 J_2(\beta_n r_m)}{r_{m+1}^2 - r_m^2} - \frac{r_m^2 J_2(\beta_n r_m) - r_{m-1}^2 J_2(\beta_n r_{m-1})}{r_m^2 - r_{m-1}^2} \right] \right\} \quad (40)$$

This concludes the description of the method used to compute sensor transcapacitance from material properties and sensor geometry.

3 EXPERIMENTAL VERIFICATION OF CYLINDRICAL COORDINATE MODEL

This section describes an experiment designed to test the cylindrical geometry method laid out in this paper. The experiment entails measurements with a pair of circular dielectrometers with different depths of sensitivity shown in Figure 1.

At the frequency of operation, 15.8 kHz, all materials used in the experiment can be treated as perfect insulators, i.e. their values of the complex permittivity ϵ^* are purely real. This means that the sensor transcapacitance is also purely real, and no useful instrument phase data are available. There is no loss of generality by working only with real ϵ, because working with complex ϵ^* results in no changes to the model.

In this experiment two unknown quantities are measured simultaneously, by combining the magnitude of the signal from the two sensors. The two unknown quantities are the permittivity of a dielectric plate positioned above the sensors, and the lift-off, defined as the distance between the bottom surface of the plate and the sensor electrode surface. The thickness of the plate is known, 1.58 mm, and is included in the model. The entire sensor assembly is contained in a metal chamber, whose cover acts as the ground plane, positioned several centimeters above the sensor and the dielectric plate. The geometric parameters of the sensors in Figure 1 are as follows (see definitions in Figure 2): $a = 1.75$ mm, $b = 4.5$ mm, $\theta = 180°$, $h = 0.254$ mm, and $\epsilon_S = 2.1$. The radial extent of the sensing electrodes of the two sensors are from $a_1 = 4.75$ to $a_2 = 5.50$ mm and from $a_1 = 9.19$ to $a_2 = 10.6$ mm, respectively.

Converting the raw sensor magnitude data to estimated parameter data is done with the help of a two-dimensional measurement grid. A measurement grid is a look-up table of precomputed transcapacitance data for a range of values for the two unknown properties [4, 5], permittivity and lift-off in this case. It is used to estimate the unknown properties from sensor data using two-dimensional inverse interpolation [1, pp. 153–161]. The advantage of this parameter estimation method over root-finding and minimization techniques is that it is much faster and more robust and therefore better suited to real-time measurements.

The measurement grid used in this experiment was generated with the semi-analytical method described and is plotted in Figure 7. The grid was computed using the model presented in this paper, with the sensor parameters and the material properties as inputs. Additionally, the model used the following values for the remaining parameters: the Fourier-Bessel Series radius $R = 20$ mm, the number of collocation points $K = 35$, and the infinite summations used $N = 5000$ Fourier-Bessel terms. A way to understand the grid qualitatively is to follow two con-

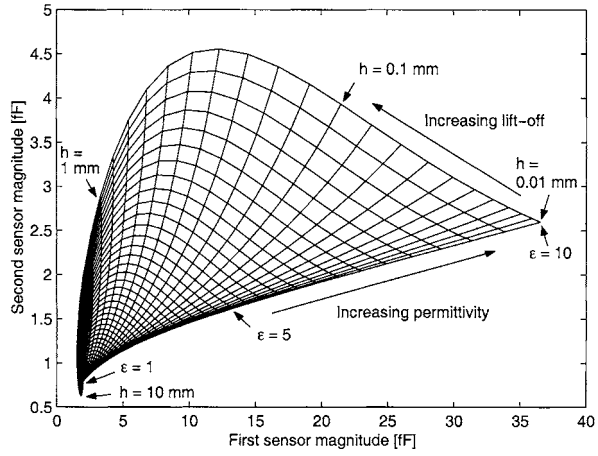

Figure 7. Permittivity/lift-off measurement grid for the pair of dielectric sensors in Figure 1. The first sensor, the left one in Figure 1, has the shorter depth of sensitivity. The thickness of the dielectric plate is fixed at 1.58 mm (1/16″). The relative permittivity range of the grid is from 1 to 10, and the lift-off range is 0.01 mm to 10 mm, both on a logarithmic scale. The Fourier-Bessel series radius $R = 20$ mm was used to calculate the measurement grid.

stant lift-off lines, for two different values of the lift-off. When the lift-off is low, the average slope of the line is low, because the magnitude of the signal of the first sensor increases much faster than the second one, since it is closer to the driven electrode. On the other hand, at higher lift-off values the lines become almost vertical, since the dielectric plate is too far from the first sensor to affect its response significantly, while some of the electric field lines that terminate on the second sensor electrode still pass through the plate.

A curious aspect of the grid in Figure 7 is that at the highest lift-off values the sensors' magnitudes actually decrease with increasing permittivity, and as a consequence in the figure the $\epsilon = 1$ point on the grid is not at the bottom left corner. This happens because at these high lift-off values while the dielectric plate is too far from the sensors for any electric field lines that terminate on the sensing electrodes to pass through it, it can still affect the response by redirecting some of the field lines that would otherwise have ended on the sensing electrodes to the grounded top plane, which is the sensor enclosure cover in this setup. This effect would not have been modeled correctly if the top plane had not been considered, which is how the models used to be formulated by others [2], where any ground reference above the material was taken to be infinitely far away. This phenomenon has also been observed experimentally.

The measurements are made with two dielectric sheets of equal thickness, 1.58 mm, made of different materials. The first one is made of polycarbonate (Lexan), with a dielectric constant of 3.2. The second one is made of material used in printed circuit boards, with a higher dielectric constant, apparently near 4.8. These two dielectric plates are suspended above the sensors with the aid of spacers at the sides, at lift-offs ranging from intimate contact, which is a few hundredths of a millimeter due to surface roughness, to about three millimeters.

The results of the measurements are listed in Table 1 and plotted on the measurement grid in Figure 8. The

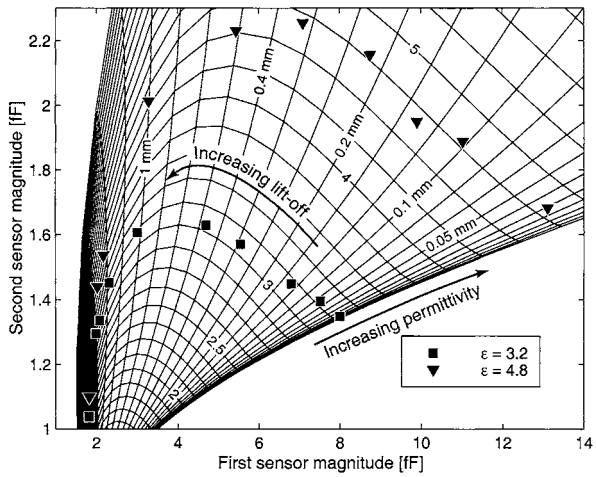

Figure 8. Results of measurements with the circular dielectric sensors. Two sets of measurements are shown with materials of different permittivity, taken at a variety of lift-off positions. Each set follows lines of constant permittivity on the measurement grid.

two groups of ten measurement sets correspond to the two different materials. It can be seen right away in the table that the task of independently measuring permittivity and lift-off has succeeded. The measured permittivity is decoupled from the varying lift-off. The accuracy of the measurement decreases significantly at high lift-off values, above approximately 1 mm. This is understandable, since at these separations very few of the electric field lines pass through the material. This can be visualized graphically by noting that the high lift-off points fall on areas of the grid in Figure 8 where the grid lines are very dense, which means that small variations of the sensor response result in large variations of the estimated properties [4].

It can be further observed in Figure 8 that the two data sets follow two separate lines of constant permittivity, closely matching the curvature of these lines. This, more than anything else, validates the correctness of the model, since it is very unlikely that a correct relationship that is so highly nonlinear could be accidental.

Table 1. Results of measurements in Figure 8 with the circular dielectric sensors, showing values for the relative permittivity (ϵ) and the lift-off (h). The nominal relative permittivity of Lexan is 3.2 and for the printed circuit board (PCB) material it is about 4.8.

	Lexan □		PCB ▽	
Data set	ϵ	h [mm]	ϵ	h [mm]
1	3.20	0.019	4.76	0.029
2	3.22	0.070	4.83	0.100
3	3.18	0.135	4.73	0.139
4	3.15	0.299	4.90	0.213
5	3.14	0.458	4.84	0.325
6	3.30	1.028	4.68	0.497
7	3.46	1.528	4.82	0.984
8	3.49	1.845	4.48	1.662
9	3.57	1.979	4.53	1.865
10	3.60	2.877	3.68	2.641

4 SUMMARY

The semi-analytical collocation point models have been successfully applied to dielectric sensors with cylindrical geometry. The dependence of the electromagnetic fields on the z-coordinate exactly parallels the Cartesian case, while the periodic sinusoidal dependence on the x-coordinate is transformed to Bessel functions of the r-coordinate in cylindrical geometry. This requires the use of Fourier-Bessel series. Although there is no periodicity in this geometry, the basic principles of the periodic sensors can still be applied by choosing a domain for the Bessel series that is much larger than the characteristic sensor dimensions.

The validity of the analysis was confirmed for the capacitive sensor by performing permittivity/lift-off measurements using two sensors with differing electric field penetration depths.

REFERENCES

[1] Y. Sheiretov, *Deep Penetration Magnetoquasistatic Sensors*, Ph.D. thesis, Department of Electrical Engineering and Computer Science, Massachusetts Institute of Technology, pp. 48-59, 69-75, 2001.

[2] M. C. Zaretsky, L. Mouayad and J. R. Melcher, "Continuum Properties from Interdigital Electrode Dielectrometry", IEEE Trans. Electr. Insul., Vol. 23, pp. 897–917, 1988.

[3] F. B. Hildebrand, *Advanced Calculus for Applications*, 2nd Edition, Prentice-Hall, Inc., Englewood Cliffs, NJ, pp. 226–230, 1976.

[4] N. J. Goldfine, *Uncalibrated, Absolute Property Estimation and Measurement Optimization for Conducting and Magnetic Media Using Imposed $\omega - k$ Magnetometry*, Sc.D. thesis, Department of Mechanical Engineering, Massachusetts Institute of Technology, pp. 75–106, 1990.

[5] N. J. Goldfine and J. R. Melcher, "Apparatus and Methods for Obtaining Increased Sensitivity, Selectivity, and Dynamic Range in Property Measurements Using Magnetometers", US patent number 5,629,621, 1997.

Ian C. Shay was born on 2 March 1970 in Sofia, Bulgaria. Dr. Shay obtained the BS, MS, EE and Ph.D. degrees in 1992, 1994, 1998 and 2001, respectively from the Massachusetts Institute of Technology, USA. He is a Senior Scientist and Lead Software Architect at JENTEK Sensors, Inc. in Waltham, MA. Dr. Shay's interests include electromagnetic field and sensor analysis and modeling; solid state infrared laser design, testing and microfabrication; power electronics; wireless telecommunications; analog and digital system design. His software development has focused on numerical methods, data modeling and analysis, robust numerical estimation on a variety of platforms, including C++, Fortran, Basic, Common Lisp, and data analysis packages such as MATLAB, Maple, Mathematica. He has interest in GUI software design for Windows, UNIX/X-Windows and Macintosh platforms. He is a recipient of the 1992 Henry Ford II Scholar Award for Academic Excellence and a member of IEEE and the Eta Kappa Nu honor society.

Markus Zahn (F'93) is the Thomas and Gerd Perkins Professor of Electrical Engineering at MIT. He received the BSEE, MSEE, the Electrical Engineers, and the Sc.D. degree degrees in 1968, 1969 and 1970, respectively all from the Massachusetts Institute of Technology. From 1970-1980 he was a Professor of Electrical Engineering at the University of Florida, Gainesville. He joined the MIT faculty in 1980. He is also the Director of the MIT Course VI-A Electrical Engineering and Computer Science Internship Program, a cooperative work/study program with Industry and Government. Since 1992 he has had numerous visiting appointments in France, Japan, and Israel (Technion) university and research centers. He was a Paris, France Sciences Scholar for 2000 and received the Ecole Superieure de Physique et de Chimie Industrielle (ESPCI) medal. He is the author of Electromagnetic Field Theory: A Problem Solving Approach (Wiley, 1979; Krieger, 1987, 2003; including translations in Spanish and Polish) and has co-developed a set of educational videotapes on Demonstrations of Electromagnetic Fields and Energy. His interests include electromagnetic field interactions with materials including the development of electromagnetic sensors, electro-optics, flow electrification, continuum electromechanics, electrohydrodynamics and ferrohydrodynamics, and micro-electromechanical systems. He is co-inventor on 13 patents plus three more patents pending related to batteries; capacitive and inductive sensors of dielectric, conduction, magnetic, charge transport, and flow electrification charging properties of media; ferrohydrodynamics; magnetometers; a method for magnetically assisted assembly of integrated circuit wafers; and detectors for buried objects such as landmines. Professor Zahn has received numerous awards for excellence in teaching, including the MIT Graduate Student Council Teaching Award in 1989 and the MIT Frank E. Perkins award for excellence in graduate student advising in 1999. He is presently serving as Associate Editor of the Transactions, Chairman of the Liquid Dielectrics Committee, and is on the International Advisory Committee of the International Conference on Dielectric Liquids. He was the 1998 J.B. Whitehead Memorial Lecturer of the IEEE Conference on Electrical Insulation and Dielectric Phenomena. He was also the First James R. Melcher Memorial Lecturer at the First Joint Meeting of the IEEE Industry Applications Society-Electrostatic Processses Committee and the Electrostatic Society of America, Little Rock, AR on June 27, 2003. He serves on the Academic Advisory Board of the W.M. Keck Laboratory for Electro-Hydrodynamics of Suspensions at the New Jersey Institute of Technology and was a member of the National Academies Naval Studies Board Committee for Mine Warfare Assessment. Prof. Zahn is a member of the MIT Humanitarian Demining Group and successfully completed the Deminers Orientation Course at the Night Vision and Electronic Sensors Directorate Countermine Division at Ft. Belvoir, Virginia in 1998.